Metallomacrocyclic–carbon complex: A study of bifunctional electrocatalytic activity for oxygen reduction and oxygen evolution reactions and their lithium-oxygen battery applications

Anupriya Arul[a], Hyoseok Pak[a], Kwang Uk Moon[a], Maria Christy[b], Mi Young Oh[b], Kee Suk Nahm[a,b,c,*]

[a] Department of Energy Storage & Conversion Engineering, Jeonju 561-756, Republic of Korea
[b] R & D Education Centre for Fuel Cell Materials & Systems, Jeonju 561-756, Republic of Korea
[c] School of Chemical Engineering, Chonbuk National University, Jeonju 561-756, Republic of Korea

A B S T R A C T

A metallophthalocyanine – carbon complex is designed by a simple approach to achieve superior, bifunctional catalytic activity. A simple and cost-effective technique is utilized to prepare carbon_iron phthalocyanine composites. Furthermore, to investigate ball milling effects, iron phthalocyanine is ball milled, which is used to prepare the carbon_ball-milled iron phthalocyanine composites. All the prepared composites exhibit better catalytic activity in both oxygen reduction and oxygen evolution reactions than Pt/C, indicating carbon support significantly improves the stability, conductivity, and surface properties of iron phthalocyanine. The ball-milling improves specific surface area, which in turn enhances the oxygen evolution reaction activity of the composites. When the carbon-iron phthalocyanine composites were applied to an air-cathode catalyst in a lithium-oxygen battery, high reversibility and low over-potential were attained. Among all the synthesized catalysts, the reduced graphene oxide_ball-milled iron phthalocyanine composite exhibits superior bifunctional electrocatalytic activity with high reversibility (92%) and low over-potential (0.7 V) due to enhanced surface properties.

1. Introduction

The rechargeable lithium-oxygen (Li-O_2) battery is an attractive candidate for the next generation energy storage devices due to their high theoretical specific energy (11,425 Wh/kg) [1]. However, there are still various critical issues to overcome in order to make them practical. Particularly, the development of effective bifunctional electrocatalysts is of crucial importance in order to achieve high efficiency and long cycle life. A bifunctional catalyst should catalyze both oxygen reduction reactions (ORR) and oxygen evolution reactions (OER) that take place in the Li-O_2 battery. During the early stage of catalyst development, various ORR catalysts have been successfully reported [2–4] whereas the development of OER catalysts is still behind. An OER catalyst should effectively decompose the solid discharge product (Li$_2$O$_2$) at a low over-potential. So far, a great deal of attention has been paid to the development of such bifunctional catalysts, which include carbons, oxides, carbides, nitrogen doped carbons and perovskites, but the low over-potential criterion is yet to be satisfied [5–8]. Hence it is necessary to develop

a suitable bifunctional catalyst that catalyzes the OER, as much as the ORR activity that takes place in the Li-O_2 system.

Among the various non-precious catalysts that are being investigated, phthalocyanine (Pc) has attracted enormous interest due to its low cost, outstanding electronic properties, and facile preparation methods [9–15]. Especially, metal phthalocyanine is capable of reducing oxygen at higher potentials and is considered the most suitable ORR catalyst [16]. Electrocatalytic studies on the ORR performance of the metal phthalocyanine have been reported over the years [16–19]. However, the poor electron conductivity and stability of phthalocyanine complexes makes them inadequate for practical applications. To overcome these issues and to enhance their ORR performance, various possible approaches are adopted, like the incorporation of nitrogen coordinates, transition metal supports, pyrolysis treatment and carbon supports. Among them, employing a suitable carbon support is considered to be a simple and cost-effective method [17,20–23]. Carbon-supported metal phthalocyanine has been verified to improve conductivity and stability, and greatly enhance ORR activity [23–26].

* Corresponding author at: School of Chemical Engineering, Chonbuk National University, Jeonju 561-756, Republic of Korea. Tel: +82 63 270 2311.
E-mail address: nahmks@jbnu.ac.kr (K.S. Nahm).

Recently, Li et al. [27] studied the ORR performance of three different types of carbon-supported phthalocyanine for fuel cells and observed excellent stability compared to commercial Pt/C. Metal phthalocyanine has been employed in various carbon supports including Vulcan carbon, ordered mesoporous carbon, graphene sheets and mesoporous carbon vesicles for various applications [27–29]. However, the synthetic methods require tedious experiments that are hard to tailor to structure and surface properties. The preparation methods also involve expensive processes, since phthalocyanine is poorly dispersed in many solvents, complicating overall synthesis.

Metal phthalocyanine as an OER catalyst has received much less attention. Abbaspour et al. [30] attempted to improve OER activity with phthalocyanine-multi-wall carbon nanotube (MWCNT) complexes in acidic and alkaline media. However, according to previous studies, the lack of proper interface between phthalocyanine and carbon makes them poor OER catalysts [27]. So, enhancement of OER activity by metal phthalocyanine remains undeveloped.

Similarly, in terms of lithium-air battery application, very few studies have been reported for phthalocyanine. In fact, phthalocyanine has been employed as a redox mediator in the electrolytes as a solution phase catalyst [22]. Only recently, Trahan et al. [31] reported cobalt phthalocyanine (CoPc) was a suitable ORR catalyst for lithium air batteries and explained the discharge chemistry of CoPc in the air-cathode. Other than that, to the best of our knowledge, utilization of phthalocyanine as a solid bifunctional (both ORR and OER) catalyst for lithium-air batteries has not been reported.

Therefore, even though phthalocyanine has been examined as a catalyst for a period of time, it still needs further detailed investigations in various areas. It is necessary to develop a facile and simple way to prepare carbon-supported metal phthalocyanine with improved ORR performance. It is also essential to find a simple and efficient way to improve the interface state between phthalocyanine and carbon and thereby to enhance their OER activity. At the same time, application studies of the metallophthalocyanine–carbon complex as bifunctional electrocatalysts in the Li-O$_2$ battery are needed to enhance battery efficiency.

In our previous work [32], we developed iron phthalocyanine (FePc) supported with graphite nanofibers (GNF) to form mesoporous cathode catalysts. The synthesized electrocatalysts showed good surface properties, electrocatalytic activities and proved to be potential electrocatalysts for Li–O$_2$ batteries. The results were published without further delay. However, to further extensively investigate this combination, to understand the relation between the metal phthalocyanine and the carbon support, and to improve the bifunctional catalytic activity (mainly OER), further studies presented in this work.

In this work, the bifunctional electrocatalytic activity of iron phthalocyanine (FePc) anchored on two different carbon supports (reduced graphene oxide [RGO] and carbon nanotube [CNT]) are extensively studied. A simple and cost-effective technique is used to prepare the RGO_FePc and CNT_FePc composites. Moreover, to enhance the OER characteristics by improving the interface between the phthalocyanine and carbon, surface properties of Pc are enhanced by ball-milling (BM). That is, FePc was ball-milled and the RGO_BM FePc and CNT_BM FePc composites are prepared in the same way. Ball-milling significantly reduced the particle size of FePc and improved the overall surface area of the composites. The electrocatalytic activity of both ball-milled (RGO_BM FePc and CNT_BM FePc) and non-milled (RGO_FePc and CNT_FePc) composites are comparatively analyzed in both aqueous and non-aqueous media. The experimental results suggest that it is possible to improve the OER activity of the carbon_FePc composites by improving their surface characteristics. Also, when applied in the non-aqueous lithium-oxygen battery system, carbon_FePc composites delivered high specific capacity and low over-potential, exhibiting improved ORR and OER activities.

2. Materials and methods

2.1. Preparation of carbon–metal phthalocyanine composites

Iron phthalocyanine (FePc, 90% purity) was commercially purchased from Sigma-Aldrich (USA) and used without further purification. Reduced graphene oxide (RGO) and carbon nanotube (CNT) were commercially purchased (Carbon Nanomaterial Technology, Co., Ltd. South Korea) and treated with 96.8 ml sulfuric acid of 98% purity and 42 ml nitric acid of 63% purity before any further processing. Carbon_FePc composite was prepared by a simple 3 step process. An equal amount (40 mg) of FePc and carbon (RGO, CNT) was dispersed in 100 ml dimethyl formamide (DMF) separately and then they were mixed together drop-wise. The mixed solution was stirred for 7 h at room temperature and ultrasonicated for 40 mins. Then the obtained carbon_FePc composites were washed with DMF and vacuum dried at 80 °C. To evaluate the effect of ball milling, a portion of FePc was ball-milled (BM) at the sample-ball ratio of 1:50 in a ball miller reactor at 250 rpm for 1 h. Carbon_BM FePc composites were also prepared by the three step process mentioned above. The as-prepared composites are named (i) RGO_FePc, (ii) RGO_BM FePc, (iii) CNT_FePc, and (iv) CNT_BM FePc.

All the material characterization techniques utilized in this study are explained in detail in the supporting information. The electrocatalytic activity of the sample was evaluated in both aqueous and non-aqueous media. A detailed description of the electrochemical characterization techniques used is also given in the supporting information.

3. Results

3.1. Physical characterisation

The structural characteristics of synthesized composites are examined by X-ray diffraction as given in Fig. 1(a). The sharp peaks at 7.0, 9.2, 18.2, 18.6, 23.9, 26, 28, 29.6, 30.6° are well indexed to characteristic FePc planes (110), (102), (302), (104), (105), (401), (314), (215), (315), respectively [JCPDS No.14-0926] [20]. After ball milling, however, the FePc diffraction peaks are much lower in intensity and form few broad peaks at 7.2° and between 22 and 27° respectively, as reported in the literature [21]. The broadening of the XRD peaks reveals the loss of FePc crystallinity due to severe plastic deformation induced by high energy ball impacts [22]. No new peak is found in the pattern, indicating that no new structure is formed during milling. CNT exhibits diffraction peaks at 2θ = 26 and 43°, which correspond to the graphitic planes of (002) and (100) [23]. RGO shows a broad peak between 2θ = 22 and 25° that corresponds to the graphitic (002) plane [24]. The synthesized composites such as RGO_FePc and CNT_FePc possess both the characteristic peaks of phthalocyanine and carbon with a slight peak position shift. A similar observation is also seen for RGO_BM FePc and CNT_BM FePc, with low-intensity diffraction peaks, as seen from the ball milled FePc. The inclusion of both the characteristic peaks is notable evidence for the proper formation of carbon_FePc composites without any other impurities. The peak position shift indicates the occurrence of monomeric FePc that are attached to carbon crystals [33]. The pristine FePc exhibits a peak at 7° that usually appears due to molecular aggregation. However, the broadening of the peak at 7° observed in the as-prepared composites discloses that FePc molecules on carbon are less aggregated [34]. The particle size of FePc was calculated by the Debye-Scherrer equation (Eq. (1)) from the XRD patterns [35].

$$D = 0.9 \frac{\lambda}{d cos\theta}, \tag{1}$$

where λ = wavelength, d = the full width at half maximum intensity of the peak, and θ = diffraction angle. The particle size of FePc in
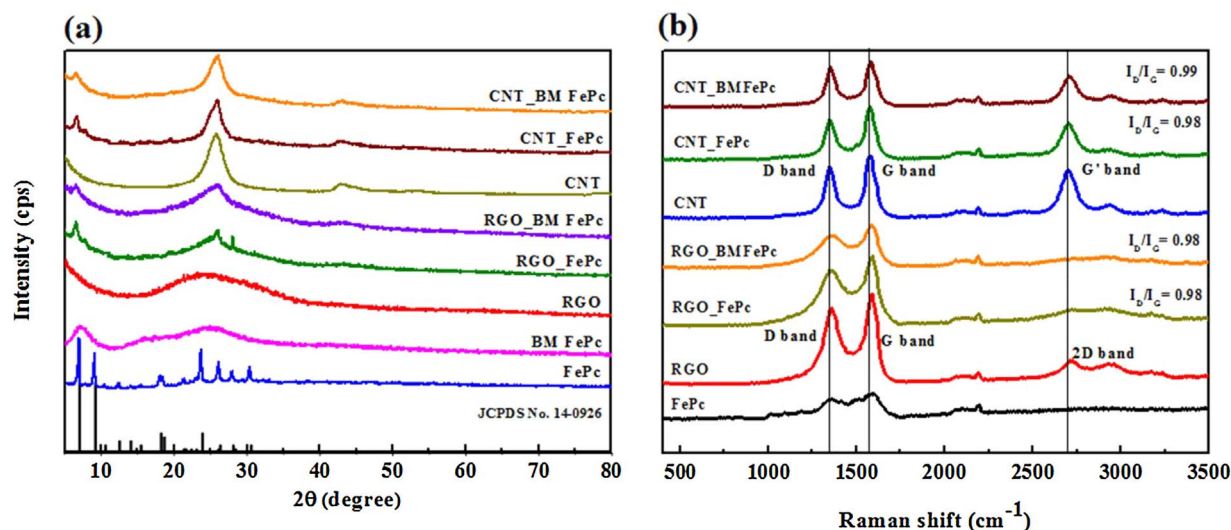
Fig. 1. (a) X–ray diffraction pattern, and (b) Raman spectra of the prepared carbon_FePc and carbon_BM FePc composites.

RGO_FePc and CNT_FePc composites are in the range of 13–20 nm, while that of RGO_BM FePc and CNT_BM FePc are calculated to be 11 nm. The calculated particle size of BM FePc from XRD patterns is consistent with the particle size obtained from TEM, as shown in Fig. 3(h).

The structural characteristics of the FePc composites are also analyzed by Raman spectroscopy given in Fig. 1(b). The characteristic D and G bands around 1336 and 1583 cm^{-1}, respectively, are found for pristine FePc and the as-prepared FePc composites [17]. The D band peak could be assigned to the vibrations of sp^3 bonded carbon atoms with defective sites while the G band indicates the sp^2 vibration of carbon atoms. Defective sites are expected to promote electron transfer and adsorb catalytic centers. The ratio of the intensity of these two bands indicates disordered structures in carbons. However, the intensity of the bands (I_D/I_G) for all the composites remains the same, indicating a proper formation of FePc–carbons. The low-intensity peaks of the prepared composites compared to the pristine RGO and CNT confirms the anchoring of FePc on carbon.

The composite structures are further investigated by Fourier transform infrared spectroscopy (FT-IR) as shown in Fig. 2(a). As observed from the spectrum of FePc, the peaks at 730 cm^{-1}, 1119 cm^{-1}, 1081 cm^{-1}, and 1467 cm^{-1} arise due to C–H bending out of plane

deformations, while the peaks at 1428 cm^{-1} and 1331 cm^{-1} emerge because of isoindole C–C stretching. These are typical characteristic peaks observed from FePc. Other characteristic peaks of FePc are observed at 1512, 1420, 1287, 1162 cm^{-1} [17]. Phthalocyanine commonly exhibits strong peaks in the region of 1000–1200 cm^{-1} because the chemical structure of the central metal atom and the molecular structure of the complexes strongly depend on this region. In this wavelength region (1000–1200 cm^{-1}), the middle peak originates from the vibration mode of a pyrrole ring, while the rest of the peaks are assigned to the in-plane deformation vibration of C–H bending in the ring [36]. Similarly, RGO characteristic peaks are observed at 1719, 1571, and 1201 cm^{-1} for (C=O) (C–O) (C=C) respectively, [37] while CNT shows its characteristic peaks at 3436, 1560, and 1166 cm^{-1} corresponding to (C=C) (C–O) (N–H) adsorption bands [38]. The synthesized composites possess both the characteristic peaks of iron phthalocyanine and carbon with no other peaks. This is again a clear evidence for the proper formation of FePc on carbon.

Thermogravimetric analysis (TGA) was used to estimate the thermal stability of the prepared composite materials. TGA was performed under an N$_2$ atmosphere at a heating rate of 5°/min up to 800 °C and the results are given in Fig. 2 (b). TGA response of FePc shows an initial loss of moisture at 100–130 °C. It is followed by an actual pyrolysis by a
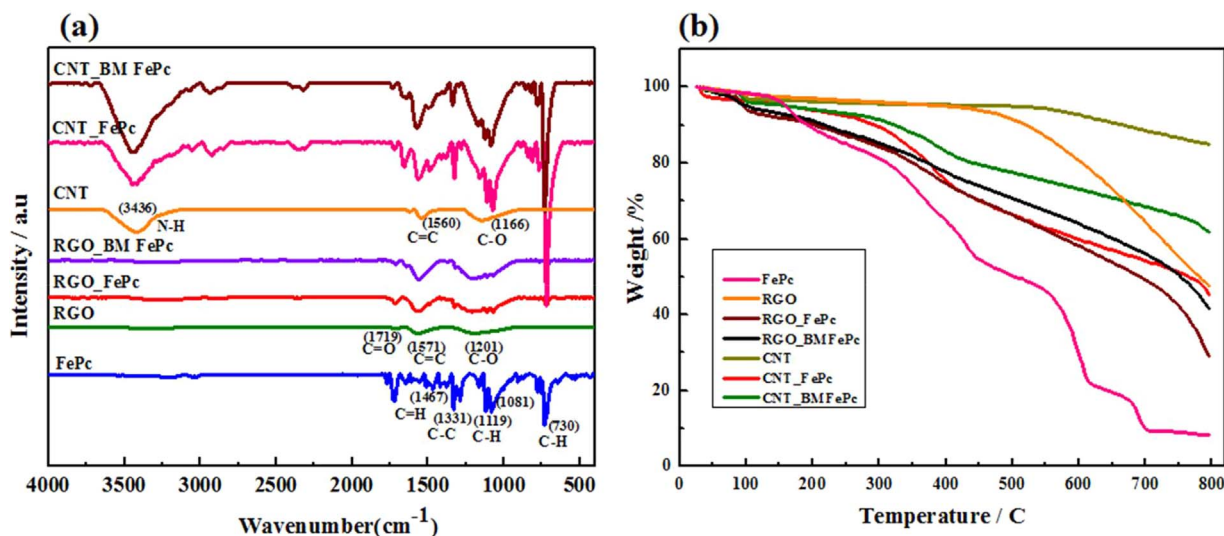

Fig. 2. (a) Fourier transform infra–red spectra, and (b) Thermogravimetric analysis of the prepared carbon_FePc and carbon_BM FePc composites.

minor decomposition at 220 °C and a major decomposition at 275 °C, resulting in low stability with fewer residual mass percentages [36]. The pristine carbon, such as CNT and RGO, shows high thermal stability with a residual weight percentage of 85% and 48%, respectively [39]. The thermal stability of as-prepared CNT composites is better than that of RGO composites regardless of ball-milling. At 800 °C, RGO composites, such as RGO_FePc and RGO_BM FePc, record mass losses of 71 and 58%, respectively, while mass losses of 55 and 38% are observed from CNT composites such as CNT_FePc and CNT_BM FePc, respectively. It is clear that the thermal stability of carbon_FePc composites is better than that of pristine FePc. At the same time, the thermal stability of carbon_BM FePc composites is better than that of carbon_FePc composites, exhibiting enhanced thermal stability. This observation is due to the fact that non-ball milled composites need lower activation energy to be vaporized, while ball milling treatment produces highly activated structures [34].

3.2. Morphology

The successful anchoring of FePc on carbon substrates is verified by field emission scanning electron microscopy (FESEM). Fig. 3 shows the FESEM micrographs of FePc-carbon composites such as, a) RGO_FePc, b) RGO_BM FePc, c) CNT_FePc and d) CNT_BM FePc. Fig. 3(a, c) shows the assorted morphologies of FePc that are loaded on the RGO and CNT surfaces. Self-assembly of FePc through intermolecular interactions is a possible reason for the diverse loading of FePc on carbon surfaces. The bonding that occurs between the aromatic structure of the carbon surface (RGO, CNT) and the macrocyclic ligand of FePc, is known as a non-covalent $\pi - \pi$ interaction [40]. Ball-milled FePc on carbon also shows a similar outcome with more particles deposited on the surface of the carbons, as shown in Fig. 3(b, d). Fig. 3[a) RGO_FePc, b) RGO_BM FePc, c) CNT_FePc, and d) CNT_BM FePc] indicates that FePc is successfully loaded on carbon [36]. For a better understanding, FESEM micrographs of FePc, BM FePc, pristine RGO, and CNT are shown in supporting information, Fig. S1.

Energy dispersive X-ray (EDX) analysis was made to identify the chemical composition of the as-prepared carbon_FePc composites (Fig. S2). EDX analysis also confirms the successful anchoring of FePc on carbon by showing the presence of Fe, C, N and O elements on the composites. The elemental analysis and their respective weight percentages are shown in the inset Table of Fig. S2.

TEM micrographs of RGO_FePc (e), RGO_BM FePc (f), CNT_FePc (g) and CNT_BM FePc (h) composites are given in Fig. 3. The inset images in Fig. 3 (g and h) show magnified micrographs for a clear presentation. From the TEM micrographs, it is clear that FePc nanodomains are loaded over the RGO and CNT. Generally, FePc strongly interacts with oxygen and oxygen functional groups to form complexes. Similarly, in this case, the loading of FePc on the carbon surface depends upon the presence of oxygen functional groups in RGO and CNT. Since RGO has a sheet-like morphology, the oxygen functional groups are present on both the sides of the sheets. In such a case, FePc could be anchored on both the sides of the RGO in RGO_FePc, as seen in Fig. 3(e). On the other hand, the large sized FePc particles seem to be present both inside and over the nanotubes of CNT_FePc (inset Fig. 3(g)). After ball milling, RGO_BM FePc composites show a large amount of smaller sized FePc on both the sides of the RGO sheet, as shown in Fig. 3(f). The CNT_BM FePc composite also exhibits a similar property, with comparatively smaller FePc particles that mostly appear inside the nanotubes, as shown in inset Fig. 3 (h). Reduction in the size of FePc after ball-milling is clearly observed in both RGO_BM FePc and CNT_BM FePc micrographs presented in Fig. 3(f, h). The inset presenting CNT_BM FePc in Fig. 3(h) shows that the inter-planar spacing and particle size of the BM FePc molecules are about 0.22 and 11 nm, respectively. The calculated particle size of BM FePc obtained from TEM is consistent with the particle size obtained from the XRD pattern. TEM micrographs confirm all the observations made from FESEM analysis.

3.3. Surface area analysis

Brunauer–Emmett–Teller (*BET*) surface area analysis was performed to determine the surface properties of the prepared composites. Fig. 4 shows the N_2 adsorption/desorption isotherm for the composites. It can be seen in Fig. 4(a–c) that the N_2 adsorption/desorption isotherm shows type IV characteristic curves, revealing that the composites have mesoporous structures. From Fig. 4(a), BM FePc (4.77 m^2 g^{-1}) shows an elevated hysteresis compared to pristine FePc (1.08 m^2 g^{-1}), indicating a four-fold increase in surface area. The RGO_BM FePc composites exhibit elevated hysteresis compared to RGO_FePc, whereas CNT_BM FePc shows only a slight elevation compared to CNT_FePc, as seen in Fig. 4(b,c). Surface properties such as specific surface area, pore
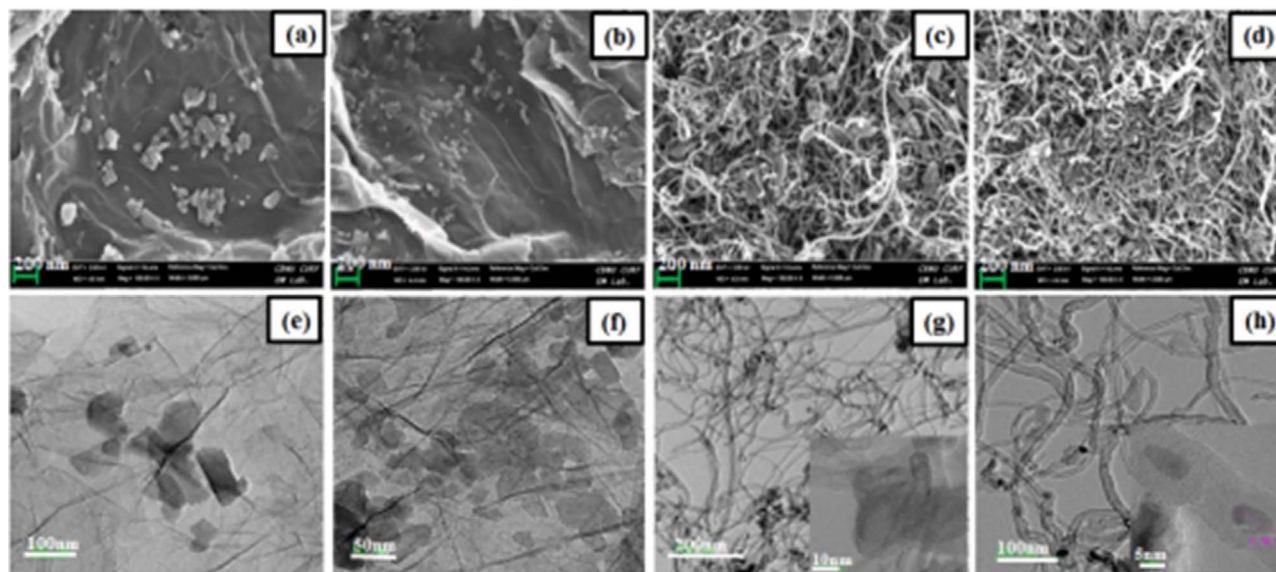

Fig. 3. Scanning electron micrographs of (a) RGO_FePc, (b) RGO_BM FePc, (c) CNT_FePc and (d) CNT_BM FePc composites; and transmission electron micrographs of (e) RGO_FePc, (f) RGO_BM FePc, (g) CNT_FePc and (h) CNT_BM FePc composites.
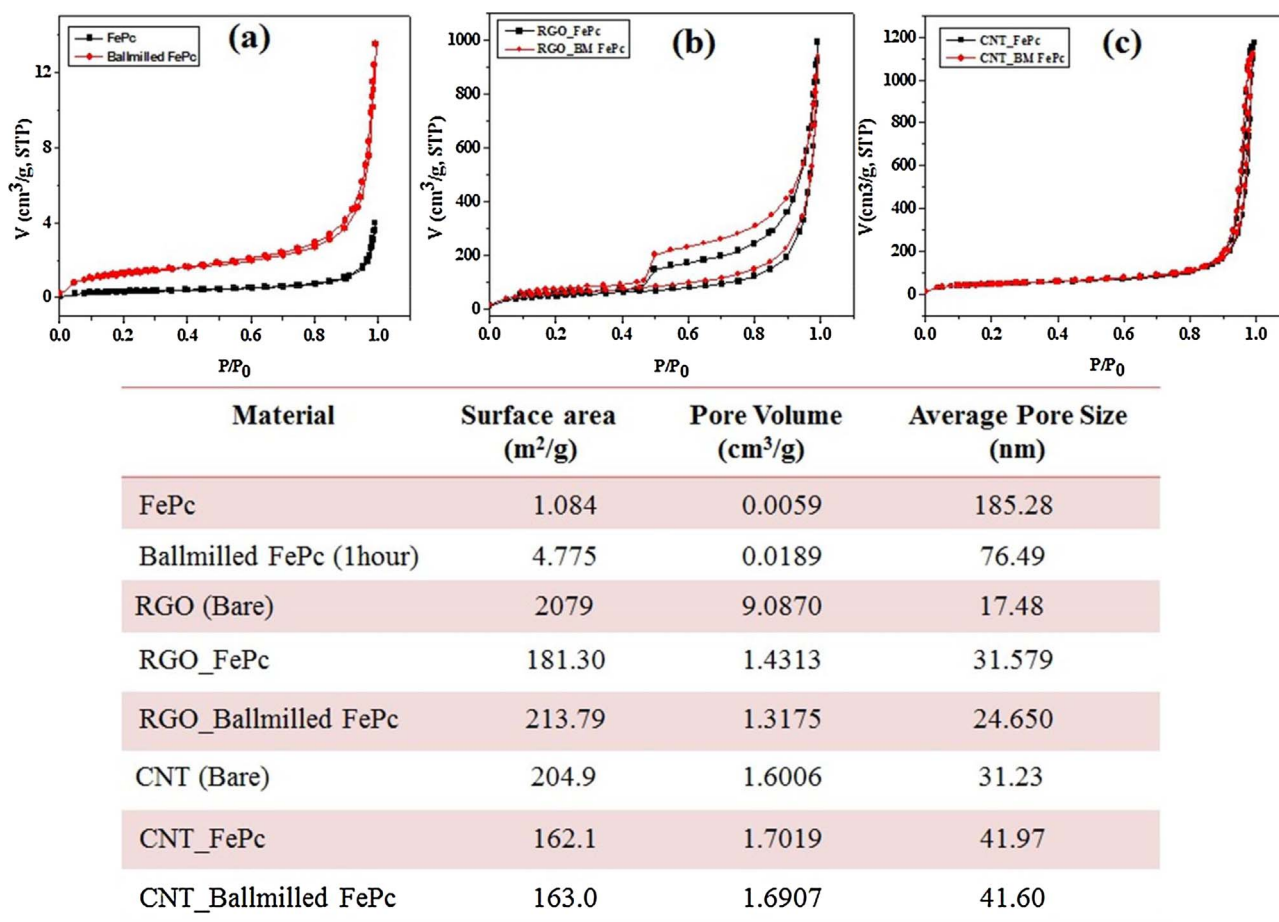
Material	Surface area (m²/g)	Pore Volume (cm³/g)	Average Pore Size (nm)
FePc	1.084	0.0059	185.28
Ballmilled FePc (1hour)	4.775	0.0189	76.49
RGO (Bare)	2079	9.0870	17.48
RGO_FePc	181.30	1.4313	31.579
RGO_Ballmilled FePc	213.79	1.3175	24.650
CNT (Bare)	204.9	1.6006	31.23
CNT_FePc	162.1	1.7019	41.97
CNT_Ballmilled FePc	163.0	1.6907	41.60

Fig. 4. N_2 adsorption–desorption isotherms of (a) FePc and BM FePc, (b) RGO composites and (c) CNT composites. Inset table summarizes the surface and pore properties of the composites.

volume, and average bare pore size, as well as prepared catalysts, are summarized in Table inset presented in Fig. 4. Bare

RGO (2079 $m^2 g^{-1}$) and CNT (204.9 $m^2 g^{-1}$) show an intrinsic high surface area and pore volume. After loading FePc, the bigger FePc particles block the pores on the surface of carbon supports such as RGO and CNT, resulting in a decreased surface area for the carbon_FePc composites. This is evidence for the successful anchoring of FePc on both RGO and CNT. Meanwhile, when compared with FePc, the synthesized carbon_FePc composites show a high surface area of about 181.3 and 162.1 $m^2 g^{-1}$ for RGO_FePc and CNT_FePc, respectively. This is because of the loading of low surface area FePc particles over RGO and CNT with high surface properties. The carbon_BM FePc composites show a slight increase in the surface area of 213.79 and 163 $m^2 g^{-1}$ for RGO_BM FePc and CNT_BM FePc, respectively. This is due to the loading of smaller BM FePc particles, which partially block the pores on the carbon surface, resulting in higher surface areas of carbon_BM FePc composites. Moreover, pore volume also increases for the prepared composites, RGO_FePc (1.43 $cm^3 g^{-1}$) and CNT_FePc (1.70 $cm^3 g^{-1}$), compared to the pristine FePc (0.0059 $cm^3 g^{-1}$). A slight decrease in pore volume is observed for carbon_BM FePc composites, which is still comparable to that of carbon_FePc (refer to Table in Fig. 4). The reduction of pore volume could be due to the aggregation of smaller particles. Nevertheless, the high surface area and pore volume obtained in the prepared catalyst materials, especially RGO composites, are expected to deliver a speedy mass transport and provide more active sites for electrocatalysis. It is also favorable for the Li-O_2 system, since the morphology and porosity of the catalyst greatly influence the capacity and rate capability of the cell [3,4].

3.4. Electrocatalytic performance

To investigate the electrocatalytic activities of the synthesized composites, linear sweep voltammetry (LSV) was performed for ORR and OER in an O_2 saturated 0.1 M KOH solution. Fig. 5(a) and (b) shows the ORR electrocatalytic activity of RGO and CNT supported composites, respectively. The onset potential, half-wave potential and limiting current values measured from the ORR curves are summarized in Table S1 in the supporting information. The electrocatalytic activity of commercial Pt/C, pristine RGO, and CNT electrodes performing under the same conditions are also included in Fig. 5 and Table S1 for comparison.

From the ORR curves in Fig. 5(a, b), the onset potentials of commercial Pt/C, pristine RGO, and CNT are measured to be −0.0040, −0.11 and −0.12 V, respectively. Compared to commercial Pt/C, the onset potentials of carbon_FePc composites are positively shifted to 0.020 and 0.018 V for RGO_FePc and CNT_FePc, respectively. The ball milled composites, RGO_BM FePc and CNT_BM FePc, exhibit onset potentials of 0.016 and 0.015 V, respectively. The half-wave potential ($E_{1/2}$) of all the prepared composites are positively shifted compared to that of the commercial Pt/C, indicating a low over-potential (ΔV) [29]. Specifically, the $E_{1/2}$ values of the carbon_FePc composites are more positive than those of the carbon_BM FePc composites. Overall, it could be inferred from the ORR results, such as onset potential and $E_{1/2}$, that the carbon_FePc composites actively participate in ORR activity with faster kinetics than the carbon_BM FePc composites. This observation is due to the presence of large pore volumes in carbon_FePc composites. The carbon_FePc composites with larger pore volume allow the deposition of reaction products on the surface of the cathode as well as
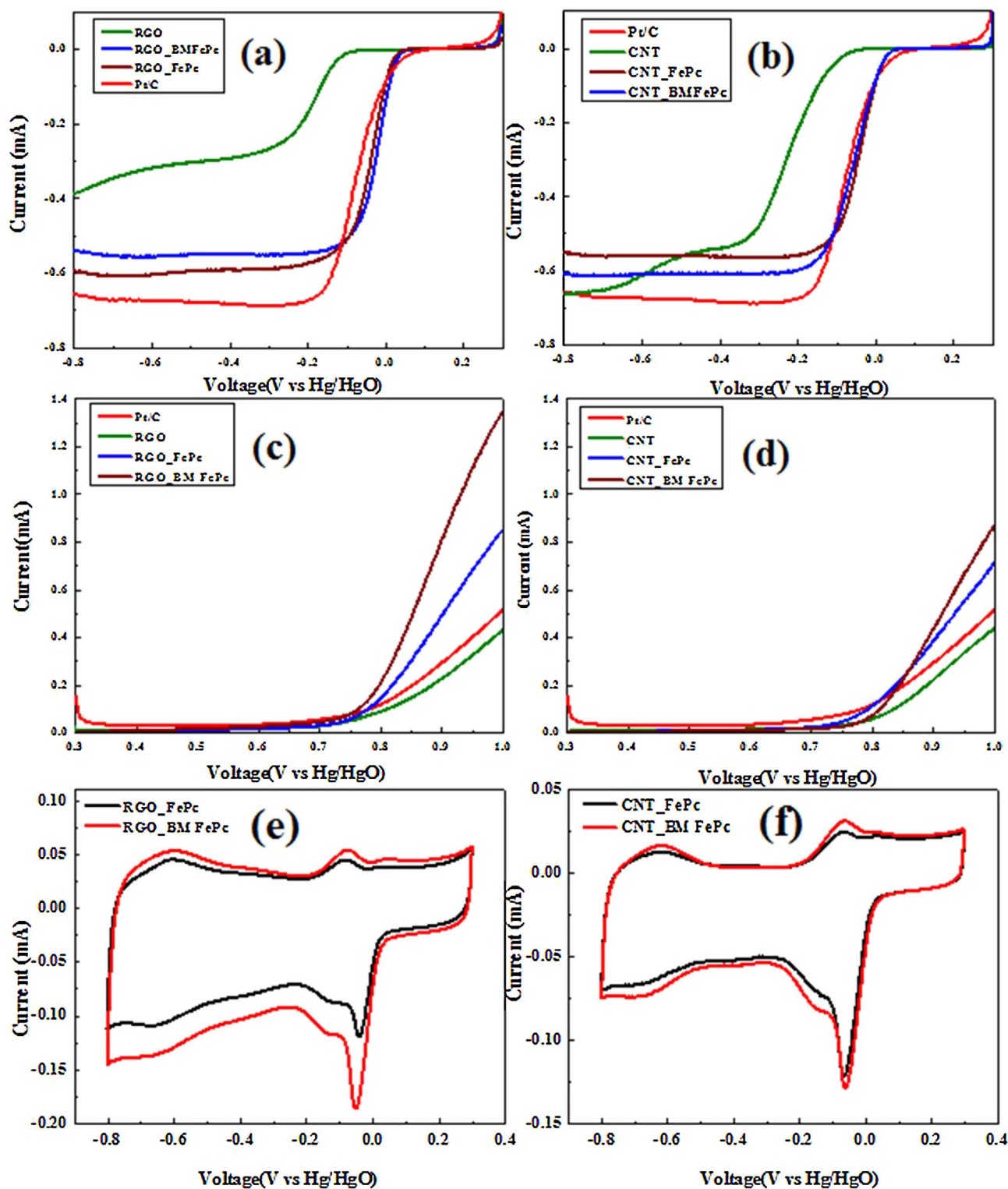
Fig. 5. Electrocatalytic performances of RGO composites and CNT composites; (a, b) LSV − ORR curves, (c, d) LSV–OER curves, and (e, f) cyclic voltammogram.

inside the pore orifices, resulting in better ORR activity. Meanwhile, the carbon_BM FePc composites with smaller pore volumes allow fewer reaction products to deposit over pore surfaces, which leads to easy decomposition entirely due to pore orifices, resulting in better OER.

The number of electrons transferred (n) during the ORR was calculated by the following equation and plotted in Fig. S3 (a) (Supporting information).

$$n = 4\left(\frac{i_D}{i_D + \frac{i_R}{N}}\right) \quad (2)$$ Here, i_D, i_R and N are disc current, ring current and

ring collection efficiency (N = 0.37), respectively. The calculated n values are found to be 3.3 and 3.7 for the pristine RGO and CNT, respectively, while n was 3.9 for all the prepared composites. An n value close to 4 indicates that the prepared composite catalysts prefer a direct one-step 4 electron transfer process.

The Tafel slope of the prepared composites was derived from the ORR LSV curves, as shown in Fig. S3(b) of the Supporting information. The Tafel slopes of RGO_FePc, RGO_BM FePc, CNT_FePc and CNT_BM FePc are found to be 52, 59, 62 and 67 mV dec^{-1}, respectively. The
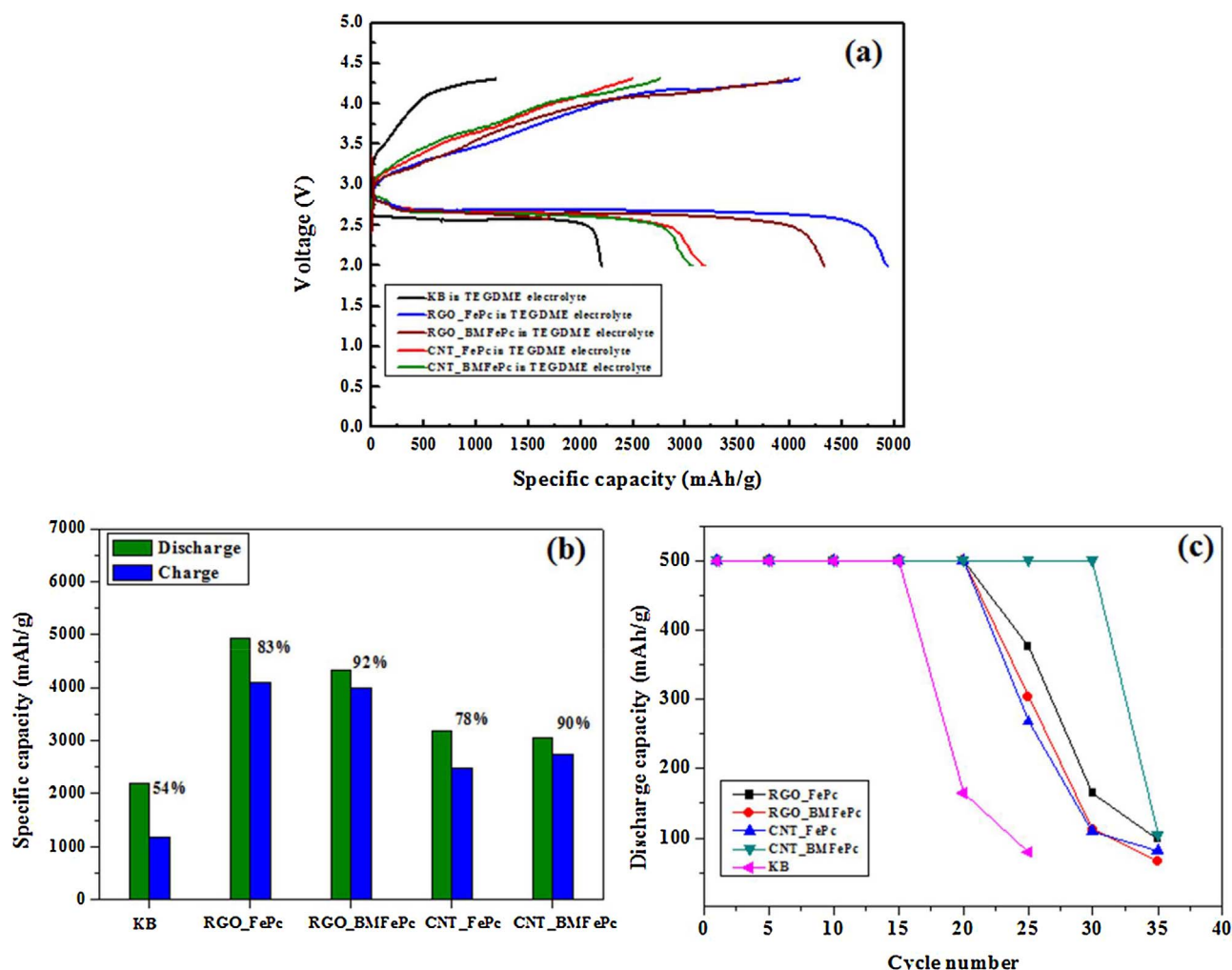
Fig. 6. Battery profiles of the prepared composite electrodes (a) first cycle discharge/charge, (b) first cycle reversibility in a bar diagram, and (c) cycle number vs. discharge capacity measured by limiting the capacity to 500 mAh g^{-1}.

small Tafel slope close to that of 60 mV dec^{-1}, reaffirms the improved ORR catalytic activity of the prepared composite catalysts due to the synergistic effect of FePc and carbon.

LSV was also carried out for OER characterization as shown in Fig. 5(c, d). All the synthesized composites exhibited better OER activity compared to the commercial Pt/C. The onset potential and current values of all the prepared catalysts, including the references such as commercial Pt/C, pristine RGO, and CNT electrodes, are given in Table S1 of the supporting information. The RGO_BM FePc displays much better OER activity than RGO_FePc, and CNT_BM FePc shows better activity than CNT_FePc. Overall, the prepared carbon_BM FePc composites exhibit superior OER performance than that of carbon_FePc composites. From the LSV ORR – OER results it is conclusive that the carbon_FePc composites promote better ORR activity, whereas the carbon_BM FePc composites deliver superior OER activity, making them bifunctional. Since carbon_BM FePc composites possess lower pore volume, this allows fewer reaction products to form on the pore orifices, which helps them to effectively decompose entire products, resulting in better OER activity. In the case of non-milled composites, the reaction products may settle deep inside the pores, making it less sufficient during OER reactions.

Fig. S4 is used to quantify the ORR and OER for the synthesized materials. The potential at which the current reaches half of its maximum value ($E_{1/2}$ = 0.5 mA) is selected for the ORR activities of the samples. Activities for the OER are judged by the potential required to

oxidize water at a current of -1.0 mA, a convention commonly used in the OER literature [41]. To assess the overall oxygen electrode activity, the difference between the OER and ORR potentials, ΔV, are tabulated. The smaller the difference, the closer the catalyst is to an ideal reversible oxygen electrode. From Table S2 of the supporting information, ΔV of all the composite catalysts are noted in the range of 0.83–0.88 V, which is better than that of Pt/C (0.92 V). The notable decrease in the ΔV value makes the prepared composites effective bifunctional catalysts suitable for Li-O$_2$ battery applications.

Fig. 5(e, f) shows the cyclic voltammogram for the prepared composites. The CV shows a strong cathodic peak and a shoulder peak at -0.05 and -0.12 V, respectively, and the subsequent anodic scan exhibits oxidation peaks at -0.07 and 0.05 V, respectively, as seen in Fig. 5 e and f. Similar observations with the main peak and a shoulder peak was also reported in the literature [27], which indicates that the strong peak is due to FePc and the shoulder peak appears when carbon content increases in the composite. The existence of the main peak was attributed to the redox reaction of Fe(II) Pc/Fe(III) Pc [27]. For the ORR, the onset potential of RGO_FePc was recorded at 0.026 V, with a peak potential of -0.039 V and a current density of -0.118 mA. However, RGO_BM FePc exhibits an ORR onset potential of 0.018 V and a peak potential of -0.050 V with a current density of -0.185 mA (Fig. 5(e)). Similarly, the onset potential of CNT_FePc was 0.017 V with a peak potential of about -0.062 V and a current density of -0.121 mA; CNT_BM FePc shows an ORR potential of 0.013 V and a peak potential of -0.059 V with a current density of -0.128 mA

(Fig. 5(f)). RGO_FePc and CNT_FePc exhibit an earlier voltage drop and current density for ORR, whereas, RGO_BM FePc and CNT_BM FePc exhibits lower onset potential and higher current density for OER. The obtained results are in a similar trend as that observed from the LSV measurements.

The stability of the prepared carbon_FePc and carbon_BM FePc composites towards ORR and OER was examined by chronoamperometry as shown in Fig. S3 (c and d) of the supporting information. The current response of the catalyst with respect to time was measured for 7200 s at a constant potential of 2.25 V, which is the voltage below the equilibrium reduction potential of oxygen. A stable current response was obtained for almost 2 h from all the cells demonstrating a better stability associated with ORR and OER. This indicates that the synthesized composites are favorable bifunctional electrocatalysts with better stability in an aqueous medium.

3.5. Li–Oxygen battery performance

Lithium-oxygen cells are tested in a potential window of 2–4.3 V at 0.1 mA cm^{-2} under 1 atm of oxygen pressure. The battery profile of carbon_FePc catalyzed cathodes along with a ketjen black (KB) cathode is shown in Fig. 6 (a). All the catalyzed Li-O$_2$ cells exhibited an open circuit voltage (OCV) of 3.3 V. Compared to the KB cathode, all the catalyzed cells exhibit overall enhanced battery profiles at full depth of discharge and charge. The discharge plateau of the composite catalysed cells was found to be 2.75 V better than that of the KB cathode at 2.65 V. KB cathodes without any catalyst deliver a first discharge capacity of 2201 mAh g^{-1} with an over-potential of 1.55 V. Meanwhile, the carbon_FePc composites catalysed cells deliver better battery performance. RGO_FePc, RGO_BM FePc, CNT_FePc, and CNT_BM FePc deliver (i) first discharge capacities of 4932, 4329, 3175 and 3052 mAh g^{-1}; (ii) first charge reversibilities of 83, 92, 78 and 90%, and (iii) over-potentials of 0.70, 0.72, 0.89 and 0.92 V, respectively. According to the first discharge capacity, the RGO composite delivers a better profile compared to CNT composites, and specifically, carbon_FePc composites deliver better ORR performance than that of carbon_BM FePc. However, on charging, the first charge capacities of RGO_FePc, RGO_BM FePc, CNT_FePc and CNT_BM FePc are found to be 4099, 3990, 2489 and 2752 mAh g^{-1}, respectively.

In terms of reversibility (Bar diagram of Fig. 6(b)), the composites shows the order of RGO_BM FePc > RGO_FePc, and CNT_BM FePc > CNT_FePc, indicating better reversibility in the carbon_BM FePc compared to carbon_FePc. However, the over-potential shows not much difference in the following order, RGO_FePc ≈ RGO_BM FePc, and CNT_FePc ≈ CNT_BM FePc, exhibiting ~0.7 and ~0.9 V for RGO and CNT composites, respectively. The obtained over-potentials are much lower than that of KB with 1.5 V. Consequently, the results indicate that the prepared FePc composites participate actively in ORR by promoting the formation of discharge products, resulting in a better discharge capacity at higher discharge potentials. On the other hand, the BM FePc composites participate actively in OER by effectively decomposing the discharge products at lower over-potentials, resulting in better reversibility.

A cyclability test was performed in the potential window of 2–4.3 V by limiting the capacity to 500 mAh g^{-1}. The cycle number vs. discharge capacity of the composite cathodes from Fig. S6 of the supporting information is plotted in Fig. 6(c). The RGO_BM FePc exhibits better cyclability for more than 28 cycles compared to RGO_ FePc; the CNT_BM FePc delivers better cyclability for more than 22 cycles compared to CNT_FePc. It is evident from the cyclability that RGO_BM FePc exhibits better cyclability and stability than all other catalysts.

4. Discussion

Electrocatalytic performance reveals efficient bifunctional catalytic activity in both alkaline and non-aqueous media. It is established that

FePc is an effective ORR catalyst with Fe central metal ion and nitrogen ligand structures [42–44]. However, the addition of a suitable carbon has efficiently improved the stability and bifunctional activity of the catalyst, as evident in Figs. 5 and 6. The non-covalent π−π bond that exists between the carbon and phthalocyanine provides the structural stability of the composites. In this study, carbon supports such as RGO and CNT are used due to their attractive intrinsic properties. The types of carbon support have quite an influence on the cathode performance. CNT has a long tubular structure and RGO a plain sheet-like morphology. FePc strongly interacts with the oxygen functional groups of the carbon to form the carbon_FePc composites. RGO with sheet-like morphology has enormous functional groups present on both its sides, which is different than CNT tubular structures. In addition, RGO also has a higher surface area than CNT. Hence it could be concluded that the RGO composites have better structural bonding and surface area properties than the CNT composites. This is the reason why the RGO composites exhibit better performance than the CNT composites. Among them, RGO_BM FePc exhibits overall superior performance in both aqueous and non-aqueous media due to its large increase in surface area.

The surface area and pore properties contribute a great deal to the better catalytic activities of the FePc composites. The carbon_FePc composites actively promote ORR activity, which is evident from the high discharge capacity and discharge potential presented in Fig. 6(a). The high surface area of the FePc composites, RGO_FePc and CNT_FePc, promotes the ORR activity by providing enormous active catalytic sites and mass transfer on the electrode surface. On the other hand, carbon_BM FePc composites exhibit a better OER activity with superior reversibility and low over-potential (Fig. 6(a)). It can be seen from the bar diagram in Fig. 6(b) that carbon_BM composites exhibit better reversibility of 92 and 90% for RGO_BM FePc and CNT_BM FePc, respectively, compared to the carbon_FePc composites (< 85%). The particle size is reduced and the specific surface area is increased for FePc after ball-milling, which results in an increase in surface area for the carbon_BM FePc composites. The comparatively lower first discharge capacity of the carbon_BM composites compared to the carbon_FePc composites could be due to the slight decrease in pore volume of the BM composites (Inset table of Fig. 4). However, the capacity is still much better than that of KB cathodes without any catalyst. It is clear that ball-milling has significantly improved the surface area, and consequently, the better OER activity of the composites. Also, ball milling has been shown to primarily change the angle between each molecule and the column axis, strengthening the π–π interaction force between FePc and carbon. Hence, the stability and OER activity is considered to be improved by ball milling.

5. Conclusions

Metallomacrocyclic–carbon complex composites, namely, RGO_FePc, RGO_BM FePc, CNT_FePc and CNT_BM FePc, were prepared by a simple process and studied as bifunctional electrocatalysts for Li-O$_2$ battery applications. The carbon-FePc composites exhibited an increase in surface area and strong π–π interaction between FePc and carbon. The electrocatalytic characterization revealed efficient bifunctional catalytic activity of the composites in both alkaline and non-aqueous media. The carbon_FePc composites actively promoted ORR activity, whereas the carbon_BM composites, promoted OER activity. Ball-milling has improved the surface area with lower pore volume and thereby improved the OER activity of the composites. It was concluded that it is also possible to improve the bifunctional activity of the catalyst by ball-milling. Among the two carbon supports, RGO exhibited better electrochemical performance. Furthermore, among the RGO composites, RGO_BM FePc exhibited superior bifunctional electrocatalytic activity due to its remarkable surface properties.

Acknowledgements

Appendix A. Supplementary data

Supplementary data associated with this article can be found, in the online version, at http://dx.doi.org/10.1016/j.apcatb.2017.08.064.

References

[1] G. Girishkumar, B. McCloskey, A. Luntz, S. Swanson, W. Wilcke, J. Phys. Chem Lett. 1 (2010) 2193–2203.
[2] A. Kraytsberg, Y. Ein-Eli, J. Power Sources 196 (2011) 886–893.
[3] A.D. Roberts, X. Li, H. Zhang, Chem. Soc. Rev. 43 (2014) 4341–4356.
[4] T.T. Truong, Y. Liu, Y. Ren, L. Trahey, Y. Sun, ACS nano 6 (2012) 8067–8077.
[5] J. Christensen, P. Albertus, R.S. Sanchez-Carrera, T. Lohmann, B. Kozinsky, R. Liedtke, J. Ahmed, A. Kojic, J. Electrochem. Soc. 159 (2011) R1–R30.
[6] L.-L. Zhang, Z.-L. Wang, D. Xu, X.-B. Zhang, L.-M. Wang, Int. J. Smart Nano Mater. 4 (2013) 27–46.
[7] Y. Shao, S. Park, J. Xiao, J.-G. Zhang, Y. Wang, J. Liu, ACS Catal. 2 (2012) 844–857.
[8] Z.-L. Wang, D. Xu, J.-J. Xu, X.-B. Zhang, Chem. Soc. Rev. 43 (2014) 7746–7786.
[9] J.C. Bommer, J.D. Spikes, Photochem. Photobiol. 53 (1991) (419-419).
[10] K. Sakamoto, E. Ohno-Okumura, Materials 2 (2009) 1127–1179.
[11] K.M. Kadish, K.M. Smith, R. Guilard, The Porphyrin Handbook: Multiporphyrins Multiphthalocyanines, and Arrays, Academic Press, 2003.
[12] P. Vasudevan, N. Phougat, A. Shukla, Appl. Organomet. Chem. 10 (1996) 591–604.
[13] X. Wang, W. Hu, Y. Liu, C. Long, Y. Xu, S. Zhou, D. Zhu, L. Dai, Carbon 39 (2001) 1533–1536.
[14] V. Bajpai, L. Dai, T. Ohashi, J. Am. Chem. Soc. 126 (2004) 5070–5071.
[15] S. Huang, L. Dai, A.W. Mau, J. Phys. Chem. B 103 (1999) 4223–4227.
[16] J. Zagal, M. Paez, A. Tanaka, J. Dos Santos, C. Linkous, J. Electroanal. Chem. 339 (1992) 13–30.
[17] C. Zhang, R. Hao, H. Yin, F. Liu, Y. Hou, Nanoscale 4 (2012) 7326–7329.
[18] L. Deng, M. Zhou, C. Liu, L. Liu, C. Liu, S. Dong, Talanta 81 (2010) 444–448.
[19] P. Vasudevan, N. Mann, S. Tyagi, Transit. Met. Chem. 15 (1990) 81–90.
[20] S. Baranton, C. Coutanceau, E. Garnier, J.-M. Léger, J. Electroanal. Chem. 590 (2006) 100–110.
[21] U.I. Koslowski, I. Abs-Wurmbach, S. Fiechter, P. Bogdanoff, J. Phys. Chem. C 112 (2008) 15356–15366.
[22] D. Sun, Y. Shen, W. Zhang, L. Yu, Z. Yi, W. Yin, D. Wang, Y. Huang, J. Wang, D. Wang, J. Am. Chem. Soc. 136 (2014) 8941–8946.
[23] Y. Jiang, Y. Lu, X. Lv, D. Han, Q. Zhang, L. Niu, W. Chen, A.C.S. Catalysis, 3 (2013) 1263–1271.
[24] R. Chen, H. Li, D. Chu, G. Wang, J. Phys. Chem. C 113 (2009) 20689–20697.
[25] G. Dong, M. Huang, L. Guan, Phys. Chem. Chem. Phys. 14 (2012) 2557–2559.
[26] R. Cao, R. Thapa, H. Kim, X. Xu, M.G. Kim, Q. Li, N. Park, M. Liu, J. Cho, Nat. Commun. 4 (2013).
[27] M. Li, X. Bo, Y. Zhang, C. Han, L. Guo, J. Power Sources 264 (2014) 114–122.
[28] T. Taniguchi, H. Tateishi, S. Miyamoto, K. Hatakeyama, C. Ogata, A. Funatsu, S. Hayami, Y. Makinose, N. Matsushita, M. Koinuma, Part. Part. Syst. Characterization 30 (2013) 1063–1070.
[29] C.W. Bezerra, L. Zhang, H. Liu, K. Lee, A.L. Marques, E.P. Marques, H. Wang, J. Zhang, J. Power Sources 173 (2007) 891–908.
[30] A. Abbaspour, E. Mirahmadi, Electrochim. Acta 105 (2013) 92–98.
[31] M.J. Trahan, Q. Jia, S. Mukerjee, E.J. Plichta, M.A. Hendrickson, K. Abraham, J. Electrochem. Soc. 160 (2013) A1577–A1586.
[32] A. Arul, M. Christy, M.Y. Oh, Y.S. Lee, K.S. Nahm, Electrochim. Acta 218 (2016) 335–344.
[33] J.P. Mensing, T. Kerdcharoen, C. Sriprachuabwong, A. Wisitsoraat, D. Phokharatkul, T. Lomas, A. Tuantranont, J. Mater. Chem. 22 (2012) 17094–17099.
[34] Y. Chen, L. Chadderton, J. Mater. Res. 19 (2004) 2791–2794.
[35] P. Scherrer, Kolloidchemie Ein Lehrbuch (Ed.), Bestimmung der inneren Struktur und der Größe von Kolloidteilchen mittels Röntgenstrahlen, Springer, 1912, pp. 387–409.
[36] Y. Gong, D. Li, Q. Fu, C. Pan, Prog. Nat. Sci. 25 (2015) 379–385.
[37] D. Zhang, T. Yan, L. Shi, Z. Peng, X. Wen, J. Zhang, J. Mater. Chem. 22 (2012) 14696–14704.
[38] X.-F. Zhang, X. Cui, Q. Liu, F. Zhang, Phys. Chem. Chem. Phys. 11 (2009) 3566–3572.
[39] A. Morozan, S. Campidelli, A. Filoramo, B. Jousselme, S. Palacin, Carbon 49 (2011) 4839–4847.
[40] C.A. Hunter, J.K. Sanders, J. Am. Chem. Soc. 112 (1990) 5525–5534.
[41] H. Jang, A. Zahoor, J.S. Jeon, P. Kim, Y.S. Lee, K.S. Nahm, J. Electrochem. Soc. 162 (2015) A300–A307.
[42] R. Taube, Pure Appl. Chem. 38 (1974) 427–438.
[43] L. Ding, X. Dai, R. Lin, H. Wang, J. Qiao, J. Electrochem. Soc. 159 (2012) F577–F584.
[44] J.H. Zagal, Coord. Chem. Rev. 119 (1992) 89–136.